Materials Advances

ROYAL SOCIETY OF CHEMISTRY

PAPER

View Article Online
View Journal

Cite this: DOI: 10.1039/d5ma01159k

Bandgap engineering for efficient perovskite solar cells under multiple color temperature indoor lighting

Miqad S. Albishi,†[a] Faisal I. Alabdulkarem,†[b] George Perrakis,†[c] Tariq F. Alhuwaymel, †[a] Ala H. Sabeeh,[de] Abdullah S. Alharbi,[a] Naif R. Alshamrani,[a] Ibrahim H. Khawaji,[de] Nikolaos Tzoganakis, [f] Majed M. Aljomah,[a] Dimitris Tsikritzis, [f] Sami A. Alhusaini,[a] Abdullah Aljalalah,[a] Kadi S. AlShebl,[a] Ali Alanzi,[a] Abrar Bin Ajaj,[g] Fay M. Alotaibi,[a] Hamad Albrithen,[ghij] Konstantinos Petridis,[h] Maria Kafesaki,[ci] Emmanuel Kymakis, [f] George Kakavelakis *[h] and Essa A. Alharbi*[a]

Perovskite indoor photovoltaics (PIPVs) are emerging as a transformative technology for low-light intensity energy harvesting, owing to their high-power conversion efficiencies (PCEs), low-cost fabrication, solution-processability, and compositionally tunable band gaps. In this work, methylammonium-free $Cs_xFA_{1-x}Pb(I_{1-y}Br_y)_3$ perovskite absorbers were compositionally engineered to achieve band gaps of 1.55, 1.72, and 1.88 eV, enabling matching of the spectral photoresponse with indoor lighting. Devices based on a scalable mesoscopic n–i–p architecture were systematically evaluated under white LED illumination across correlated color temperatures (3000–5500 K) and light intensities from 250 to 1000 lux with an active area of 1 cm^2. The 1.72 eV composition exhibited the most promising performance across different light intensities and colors, achieving PCEs of 35.04% at 1000 lux and 36.6% at 250 lux, with a stable device operation of over 2000 hours. On the other hand, the 1.88 eV band-gap variant reached a peak PCE of 37.4% under 250 lux (5500 K); however, performance trade-offs were observed across different color light LEDs. Our combined experimental and theoretical optical–electrical simulations suggest that decreasing trap-assisted recombination in wide-bandgap compositions may further improve PIPV performance across the different illumination conditions. In contrast, devices with 1.55 eV band gap underperformed in such conditions due to suboptimal spectral overlap and utilization. These findings establish bandgap optimization and device architecture as key design principles for high-efficiency, stable PIPVs, advancing their integration into self-powered electronic systems and innovative indoor environments.

Received 9th October 2025,
Accepted 12th March 2026

DOI: 10.1039/d5ma01159k

rsc.li/materials-advances

Introduction

Perovskite solar cells (PSCs) are emerging as a transformative technology within the field of photovoltaics, attracting substantial interest due to their impressive advancement in power conversion efficiency (PCE), which has reached 27% under standard outdoor solar illumination.[1,2] Beyond outdoor applications, PSCs are increasingly recognized as a viable

[a] Microelectronics and Semiconductor Institute, King Abdulaziz City for Science and Technology (KACST), Riyadh, 11442, Saudi Arabia. E-mail: ealharbi@kacst.gov.sa
[b] Sustainable Energy Technologies Center, College of Engineering, King Saud University, Riyadh, Saudi Arabia
[c] Institute of Electronic Structure and Laser (IESL), Foundation for Research and Technology – Hellas (FORTH), 70013 Heraklion, Crete, Greece
[d] Energy, Industry, and Advanced Technologies Research Center, Taibah University, Madinah, Saudi Arabia
[e] Department of Electrical Engineering, College of Engineering, Taibah University, Madinah, Saudi Arabia
[f] Department of Electrical & Computer Engineering, Hellenic Mediterranean University (HMU), Heraklion 71410, Crete, Greece
[g] Physics and Astronomy Department, College of Science, King Saud University, Riyadh 11451, Saudi Arabia
[h] Department of Electronic Engineering, School of Engineering, Hellenic Mediterranean University, Romanou 3, Chalepa, Chania, Crete GR-73100, Greece. E-mail: kakavelakis@hmu.gr
[i] Department of Materials Science and Engineering, University of Crete, 70013 Heraklion, Crete, Greece
[j] King Abdullah Institute for Nanotechnology, King Saud University, Riyadh 11451, Saudi Arabia
† These authors contributed equally to this work.

candidate for indoor photovoltaics (IPVs), owing to their tunable energy bandgap (E_g), high specific power output, and exceptionally high absorption coefficients.[3,4] This adaptability enables effective energy harvesting under various indoor lighting conditions, including light-emitting diode (LED) lamps and compact fluorescent lamps (CFLs).[3–6] Nevertheless, it is essential to note that the Shockley–Queisser (SQ) limit applicable under indoor lighting conditions diverges from the outdoor limit of approximately 33% for a bandgap of 1.34 eV. For IPVs, the SQ limit exceeds 50%, requiring E_g in the range of 1.7–2.0 eV to align with the narrowband emission spectrum (400–700 nm), a characteristic of indoor lighting.[7–9] Perovskite indoor photovoltaics (PIPVs) due to their high PCE in such illumination conditions offer opportunities for a wide range of applications, including powering internet of things (IoT) devices, wireless sensors, wearable health monitors, and smart home actuators.[10,11] One promising strategy for achieving an optimal E_g of 1.7–2.0 eV is compositional engineering, specifically through the manipulation of the X-site in the ABX_3 perovskite structure.[12] Numerous studies have focused on varying the bromide content (*i.e.*, the iodide-to-bromide ratio in the perovskite composition), resulting in a PCE of 27% with an E_g of 1.61 eV and a PCE of 33% with an E_g of 1.77 eV under indoor LED illumination at 1000 lux.[13–15] Another practical approach involves interface engineering, aimed at reducing defects through surface and bulk passivation methods, leading to reported PCEs exceeding 40%. Specifically, a PCE of 44.72% with an E_g of 1.71 eV represents the highest value reported to date in perovskite IPVs.[16–21] However, such exceptional PCE results have been achieved using small-area devices (0.09–0.1 cm^2),[22] thus emphasizing the necessity of scaling to larger active areas ($\geq$1 cm^2) for practical IPV applications, which would provide sufficient power input to drive external devices effectively. Furthermore, most of the previously reported research involves perovskites that incorporate highly volatile A-cations (including the aforementioned), such as methylammonium, while facilitating a wider material E_g, compromising device stability.[23–25] Additionally, it is noteworthy that the substantial majority of existing literature on PIPVs is centered on the p–i–n device configuration, which has demonstrated high and stable certified PCEs under both outdoor and indoor illumination.[25–47] However, there is a lack of robust evidence suggesting that this configuration (p–i–n) presents a scalable solution for the industrialization of PIPVs, particularly when contrasting with the proven scalability of the n–i–p device configuration, which involves the use of a scalable, cost-effective and eco-friendly fluorine-doped tin oxide (FTO) transparent electrode and titanium dioxide (TiO_2) electron transporting layer. In contrast, the p–i–n devices employ indium tin oxide (ITO) despite the various limitations associated with it, including cost, thermal stability, and indium toxicity.[28,29] Moreover, the extensive characterization and testing of perovskite IPVs in prior studies have predominantly employed warm white LED (WLED) light (3000 K).[48,49] At the same time, indoor environments often encompass a diverse array of lighting conditions.[48,49] Therefore, it is crucial to assess the performance of PIPVs under various color temperatures to ensure consistent operational efficacy for indoor settings. White LEDs are widely utilized as the primary indoor lighting source, principally due to their efficiency and longevity.[50,51] Their color temperature (CT) ranges from warm (2700–3500 K) to neutral (3500–4500 K) and cool (above 4500 K). Warm light tends to exhibit a redshift, in contrast to the blue shift associated with cool light. These spectral variations inherently influence the performance of any photovoltaic device, including perovskite IPVs.[16]

Herein, this study investigates the influence of varying E_g (1.55 eV, 1.72 eV, and 1.88 eV) of metal halide perovskite materials, specifically through the modulation of the iodide-to-bromide (I/Br) ratio within the perovskite composition, on photovoltaic performance under indoor lighting conditions. To enhance stability and avoid the use of volatile A-cations, a methylammonium (MA)-free perovskite formulation incorporating cesium (Cs) and formamidinium (FA) as A-cations was optimized.[52,53] This approach has not been previously employed for PIPV applications, although it has demonstrated promising results for stable PSCs under outdoor solar illumination. The investigation further encompassed the use of WLED illumination at correlated CTs of 3000 K, 4000 K, and 5500 K, across varying light intensities, to explore the effects of incident light spectrum and perovskite E_g. A theoretical framework was established through comprehensive optical full-wave electromagnetic simulations, electrical drift-diffusion modeling, and detailed analysis based on the Shockley–Queisser limit across a spectrum of E_g, CTs, and light intensities. This multifaceted approach provided essential insights into the physical mechanisms that constrain the indoor PCE of PIPV under diverse lighting conditions. The combined experimental and simulation results underscore the need to optimize PSC design for consistently high PCEs across various indoor environments. By adjusting the perovskite E_g to 1.88 eV through precise I/Br ratio manipulation, a stable indoor PCE of 37.4% was obtained under illumination of 250 lux and a CT of 5500 K utilizing a scalable and stable n–i–p device configuration, which remains largely unexplored in the context of IPVs. Additionally, a series of characterization techniques was employed to elucidate the critical morphological, compositional, electrical, and optical properties of the optimized materials and devices.

Results and discussion

To establish a robust baseline for perovskite composition and device configuration with a focus on long-term stability and upscaling potential, the present study concentrates on the long-term stable formamidinium-cesium-based perovskite composition and the n–i–p mesoscopic PSCs (*i.e.* FTO/c-TiO_2/m-TiO_2/$Cs_xFA_{1-x}Pb(I_{1-y}Br_y)_3$/SpiroOMeTAD/Au, where x = 0.10–0.15 and y = 0.02–0.85). The emission spectra of white light-emitting diodes (LEDs) featuring various CTs and intensities, as well as the spectral power irradiance utilized in this investigation, are depicted in Fig. S1 and S2.

Photoluminescence (PL) spectra were systematically collected and analyzed to determine the resulting E_g of those

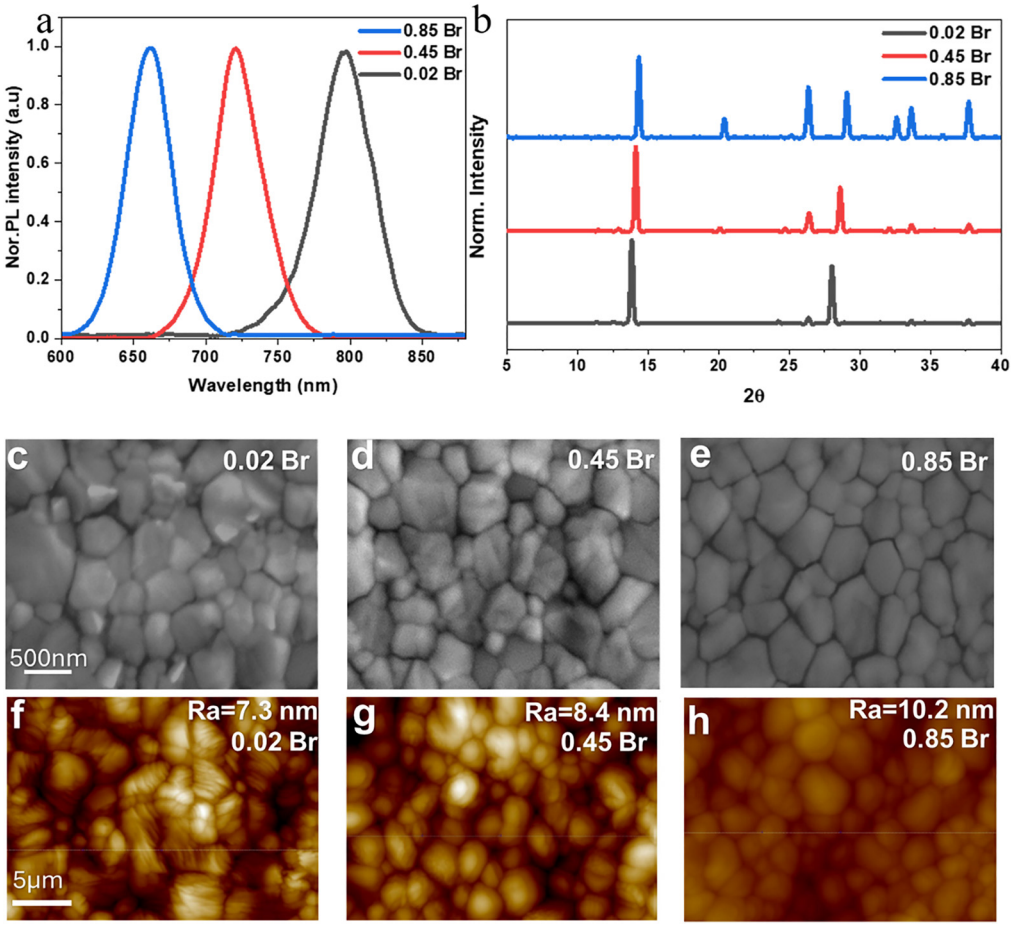

Fig. 1 (a) PL spectra, (b) XRD patterns, (c)–(e) SEM images, and (f)–(h) AFM images of perovskite films.

mixed halide perovskites by varying the I/Br ratio. As illustrated in Fig. 1a, the film, $FA_{0.90}Cs_{0.10}Pb(I_{0.98}Br_{0.02})_3$, exhibited a peak emission wavelength around 800 nm, corresponding to an E_g of 1.55 eV. As the bromine concentration increased, the films $FA_{0.85}Cs_{0.15}Pb(I_{0.55}Br_{0.45})_3$ and $FA_{0.85}Cs_{0.15}Pb(I_{0.15}Br_{0.85})_3$ displayed emission peaks at 720 nm and 662 nm, yielding bandgaps of 1.72 eV and 1.88 eV, respectively. Thus, these results confirm the successful identification of three distinct E_g (1.55 eV, 1.72 eV, and 1.88 eV).[42,43,54] Furthermore, the UV-vis absorption (Fig. S5) confirms our band gaps with absorbance shifting to shorter wavelengths from 805 nm to 730 nm and 666 nm, and therefore wider E_g energy.

Subsequent X-ray diffraction (XRD) measurements were performed to elucidate the impact of the I/Br ratio on crystallinity and phase purity across different films. Fig. 1b shows a minor peak at 11.6° for samples with 2% and 45% Br, which is associated with the δ-phase perovskite of $FAPbI_3$.[26,27,52,55] Furthermore, another weak peak at 12.6° in the 2% Br and 45% Br films corresponds to the PbI_2 peak. In contrast, the δ-phase and PbI_2 peak are absent in the 85% Br film, indicating a fully reacted final composition with no double phase coexistence.[30,56,57] The very small intensity of the δ-phase and PbI_2 peaks in the 2% and 45% Br-content perovskite films and also their absence in the 85% Br-content perovskite film indicate successful incorporation of Br in the perovskite lattice, which did not negatively affect the purity and stability of the crystal. A noticeable peak shift is observed from 13.8° for the 2% Br film to 14.1° and 14.3° for the 45% and 85% Br films, respectively, and the associated (Bragg law $d = n\lambda/2\sin\theta$) lattice parameter reduction from 6.40 to 6.17 Å over the entire compositional range under study implying a *trans* formation of the crystal structure from a tetragonal to a cubic phase.[58–60] Additionally, different peaks at 20°, 28°, and 32° in the 45% Br and 85% Br films suggest increased Br content in the perovskite-based composition.[54,59,61]

To further assess and investigate the influence of the I/Br ratio on the morphology of the perovskite films, top-view scanning electron microscopy (SEM) images were obtained for films with Br contents of 2%, 45%, and 85% (Fig. 1c–e). The SEM analysis reveals that all films maintain a compact, pinhole-free morphology, which is crucial for the fabrication of high-performance solar cells. Notably, as the Br content increases, a corresponding decrease in grain size is observed, implying that higher bromide content may enhance the rate of crystallization.[62] These morphological observations are corroborated by electrical simulations presented in the "Optical–Electrical modeling" section of the SI, which indicate a reduction in carrier lifetime at elevated bromide concentrations, an effect

anticipated to limit the maximum attainable indoor PCE. Additionally, atomic force microscopy (AFM) measurements for the perovskite films (Fig. 1f–h) show surface roughness (R_a) values of 7.3, 8.4, and 10.2 nm for the samples with 2%, 45%, and 85% Br content, respectively. A rougher absorber layer is beneficial for light trapping and minimizing reflectance losses; however, it may also adversely affect device performance due to the presence of voids.[56,63,64]

The thickness of the perovskite active layer, primarily governed by the concentration of the precursor solution,[65,66] was investigated to determine the optimal parameters for PIPV devices. Specifically, devices utilizing the composition $FA_{0.90}Cs_{0.10}Pb(I_{0.98}Br_{0.02})_3$ (E_g of 1.55 eV) were fabricated with precursor concentrations varying from 0.9 to 1.4 M. As detailed in Table S1, the PCE values were recorded as follows: 25.85% for 0.9 M, 27.07% for 1.1 M, 26.98% for 1.2 M, 30.05% for 1.3 M, and 29.46% for 1.4 M, measured at an illumination level of 1000 lux. The highest PCE of 30.05% was achieved at a precursor concentration of 1.3 M, which corresponded to a short-circuit current density (J_{sc}) of 121.4 μA cm^{-2}, an open circuit voltage (V_{oc}) of 0.897 V, and a fill factor (FF) of 76.73% under illumination at 3000 K. The optimal layer thickness was determined to be within the range of 300–400 nm,[67–69] as depicted in Fig. 2a–c, which is consistent with the simulation results illustrated in Fig. S3.

After determining the optimal perovskite precursor concentration corresponding to film thickness, a constant concentration of 1.3 M was utilized for 1.55 eV E_g, along with other compositions featuring E_g of 1.72 eV and 1.88 eV. Subsequently, the solar cells were evaluated under various CTs of 3000 K, 4000 K, and 5500 K, as well as under light intensities of 1000, 500, and 250 lux, as depicted in Fig. S2.

The devices with a 1.55 eV bandgap (Fig. 2d–f and Table S3) demonstrated V_{oc} ranging from 0.82 to 0.90 V, with the J_{sc} exhibiting a linear relationship with light intensity. At an illumination level of 1000 lux, J_{sc} was 128.1 μA cm^{-2}, while it decreased to 31.9 μA cm^{-2} under dim lighting at 250 lux, indicating efficient current scaling. Among the varying color temperatures, the highest J_{sc} was recorded under 4000 K illumination, corresponding to a greater irradiance of 3.05 W m^{-2}. In comparison, reduced values were observed at both 3000 K and 5500 K due to diminished spectral overlap. The FF remained relatively constant, ranging from 75.0% to 79.7%, resulting in PCEs of 30% at 1000 lux (3000 K) and 31.3% at 250 lux (3000 K with an irradiance of 68 W m^{-2}). The PCEs were approximately 28% under both 4000 K and 5500 K conditions. Although the intermediate data at 500 lux followed similar trends (Table S3), the lower V_{oc} limited efficiencies compared to higher bandgap devices. This outcome corroborates previous findings suggesting that lower band gaps are suboptimal for indoor conditions.[31,48] For the devices with a 1.72 eV bandgap (Fig. 2g–i and Table S4), higher current and voltage were observed. The V_{oc} values varied from 0.92 to 1.01 V, with J_{sc} reaching 132.1 μA cm^{-2} under 1000 lux (4000 K), reducing to 33.5 μA cm^{-2} under 250 lux. The FF remained almost constant, ranging from 74.6% to 78.5%. At 1000 lux, the efficiencies ranged from 32.2% to 35.0%, with a peak PCE of 35.04% achieved at 3000 K. At the level of 250 lux, the devices reached even higher efficiencies, achieving a PCE of 36.6% at 5500 K. The efficiency data at 500 lux mirrored these trends, maintaining values between 33.5% and 34.6% across all CTs. This bandgap (1.72 eV) exhibited reliable high efficiencies under various CTs and intensities, aligning with predictions that band gaps within the range of 1.70–1.80 eV are optimal for indoor photovoltaic applications[32–35] and consistent with reports indicating efficiencies exceeding 40% under LED lighting following passivation and compositional adjustments.[36–39]

The 1.88 eV devices (Fig. 2j–l and Table S5) displayed the highest V_{oc} values, ranging from 0.96 to 1.04 V. However, the current densities remained relatively low, peaking below 126 μA cm^{-2}, attributed to the reduced absorption of red photons. This phenomenon was most pronounced under 3000 K light, which contains a higher proportion of red wavelengths; however, it was less evident under 4000 K to 5500 K light, which is richer in blue photons.[40] The FF values for this bandgap were recorded between 67.4% and 74.9%. The PCE varied from 29.20% (3000 K, 1000 lux) to 37.44% (5500 K, 250 lux); this PCE is competitive with the highest values reported for perovskite indoor PVs of similar active area. Under lower illumination conditions of 250 lux (irradiance between 68 and 76 W m^{-2}), they presented superior performance under cooler white lighting, supporting findings from studies focused on optimizing perovskites for high CT light sources.[41]

To further explore these observations and understand practical constraints on PIPV performance, we conducted quantitative device simulations using optical full-wave electromagnetic modeling and electrical drift-diffusion modeling based on the finite element method (see "Optical–Electrical modeling" section in the SI).[70–76] Optical simulations provided spatially resolved charge-carrier generation profiles for various WLED CTs (3000, 4000, and 5500 K), illumination intensities (1000, 500, and 250 lux), and perovskite bandgaps (1.55, 1.72, and 1.88 eV). These generation profiles were input into the electrical model to solve the steady-state Poisson and continuity equations, yielding the simulated J–V curves in Fig. 2d–l.

To ensure quantitative agreement with experimental data, the model incorporated Shockley–Read–Hall trap-assisted recombination,[77–79] where carrier lifetimes were calibrated against experimental data for each bandgap,[80–82] yielding values ranging from 20 to 55 ns. These values align with several theoretical and experimental studies on IPVs.[78,80,83] Moreover, the simulated J–V curves (dashed) show good agreement with experimental data (solid), with modeled J_{SC}, V_{OC}, FF, and maximum power output following the experimental trends as a function of CT and illumination level.

Slight underestimation of J_{SC} in the simulations is primarily due to the abrupt absorption cutoff at the bandgap wavelength (used to avoid inconsistencies in sub-bandgap optical data across materials). Additionally, the rougher surfaces observed in the experimental devices (Fig. 2a–c) also enhance absorption compared to the idealized planar interfaces assumed in the model.[84] Importantly, the extracted carrier lifetime for the

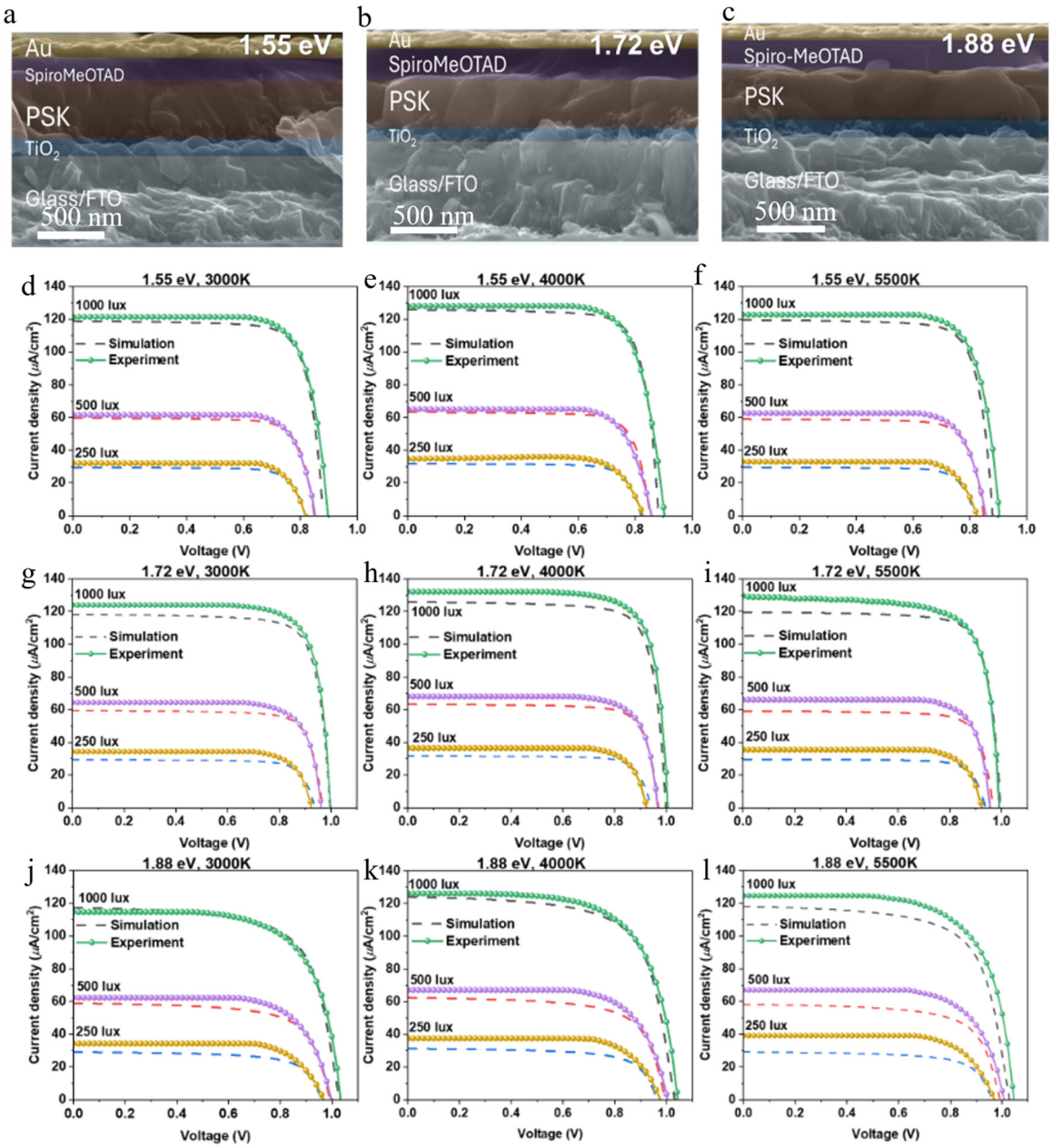

Fig. 2 (a)–(c) Cross-sectional SEM images of the corresponding cells with different bandgaps. (d)–(l) Experimental (solid) and simulated (dashed) J–V curves of perovskite solar cells with bandgaps of 1.55, 1.72, and 1.88 eV under 3000 K, 4000 K, and 5500 K indoor light (250–1000 lux).

1.88 eV devices was approximately 20 ns, compared to ~50 ns for the 1.55 and 1.72 eV cases, leading to a reduction in maximum attainable V_{OC}, which produces higher V_{oc} deficits. This shorter lifetime correlates with the smaller grain sizes observed at higher bromide content (see Fig. 1), indicating reduced carrier lifetime as a key limiting factor in the maximum attainable performance of wide-bandgap PIPVs. One way to overcome such problems and further improve indoor PCEs in the future might be to try optimizing and increasing the grain size of wide band gap perovskites. This could lead to indoor PCEs close to the efficiency limit.

Overall, the simulations predict higher indoor PCEs for the 1.72 eV devices, in agreement with experimental results. This behavior is attributed to (i) efficient spectral matching, arising from both efficient optical absorption within the incident photon spectral range (Fig. S5a and b), yielding ~94% of the SQ-limit J_{SC} (Fig. S4b), and a wider band gap than the 1.55-eV device (higher output voltage), combined with (ii) lower V_{OC} deficits than the 1.88-eV device (Fig. S5c).

Importantly, the extracted carrier lifetime for the 1.88 eV devices was approximately 20 ns, compared to ~50 ns for the 1.55 and 1.72 eV cases, leading to a reduction in maximum attainable V_{OC}, which produces higher V_{OC} deficits.[85,86] Comparisons of experimental and simulated V_{OC} with SQ-limit calculations (Fig. S6c and d) show that while both the SQ-limit and experimental/simulated V_{OC} increase from 1.55 to

1.72 eV, the increase from 1.72 to 1.88 eV is ~8.5% smaller in the experimental/simulated cases (Fig. S6c). Simulations assuming equal carrier lifetimes (~50 ns) for all band gap cases follow the SQ-limit trend (~12% improvement from 1.72 to 1.88 eV; Fig. S6c), confirming the important role of carrier lifetime. Varying the carrier mobilities (2–200 cm^{-2} V^{-1} s^{-1}) shows no substantial effect on V_{OC} (< ~3%; Fig. S6d), indicating that the reduced PCE at higher band gaps is primarily due to increased nonradiative recombination rather than charge-transport limitations. This conclusion is further supported by the smaller grain sizes observed at higher bromide content (see Fig. 1), indicating reduced carrier lifetime as a key limiting factor in the maximum attainable performance of wide-bandgap PIPVs.

Statistical analysis of the device performance reveals significant differences among the three examined band gaps. The data for each bandgap device incorporate performance metrics measured under all three WLED spectra. The devices with a bandgap of 1.55 eV (Fig. 3a) exhibited photocurrents of 123.9 ± 5.4 μA cm^{-2} at 1000 lux, alongside fill factors of 76.6 ± 1.5% and a V_{oc} of 0.87 ± 0.02 V. The corresponding efficiencies recorded were 28.7 ± 1.5% at 1000 lux, 28.5 ± 1.2% at 500 lux, and 31.2 ± 1.0% at lower illumination levels (250 lux). In contrast, the devices with a 1.72 eV bandgap (Fig. 3b) demonstrated a superior performance profile, achieving a higher V_{oc} of 0.99 ± 0.02, a J_{sc} of 123.5 ± 4.5 μA cm^{-2} at 1000 lux, and a consistent FF of 76.0 ± 2.0%. This configuration resulted in efficiencies of 32.8 ± 1.2% at 1000 lux, 31.8 ± 3.2% at 500 lux, and 33.7 ± 1.9% at 250 lux.

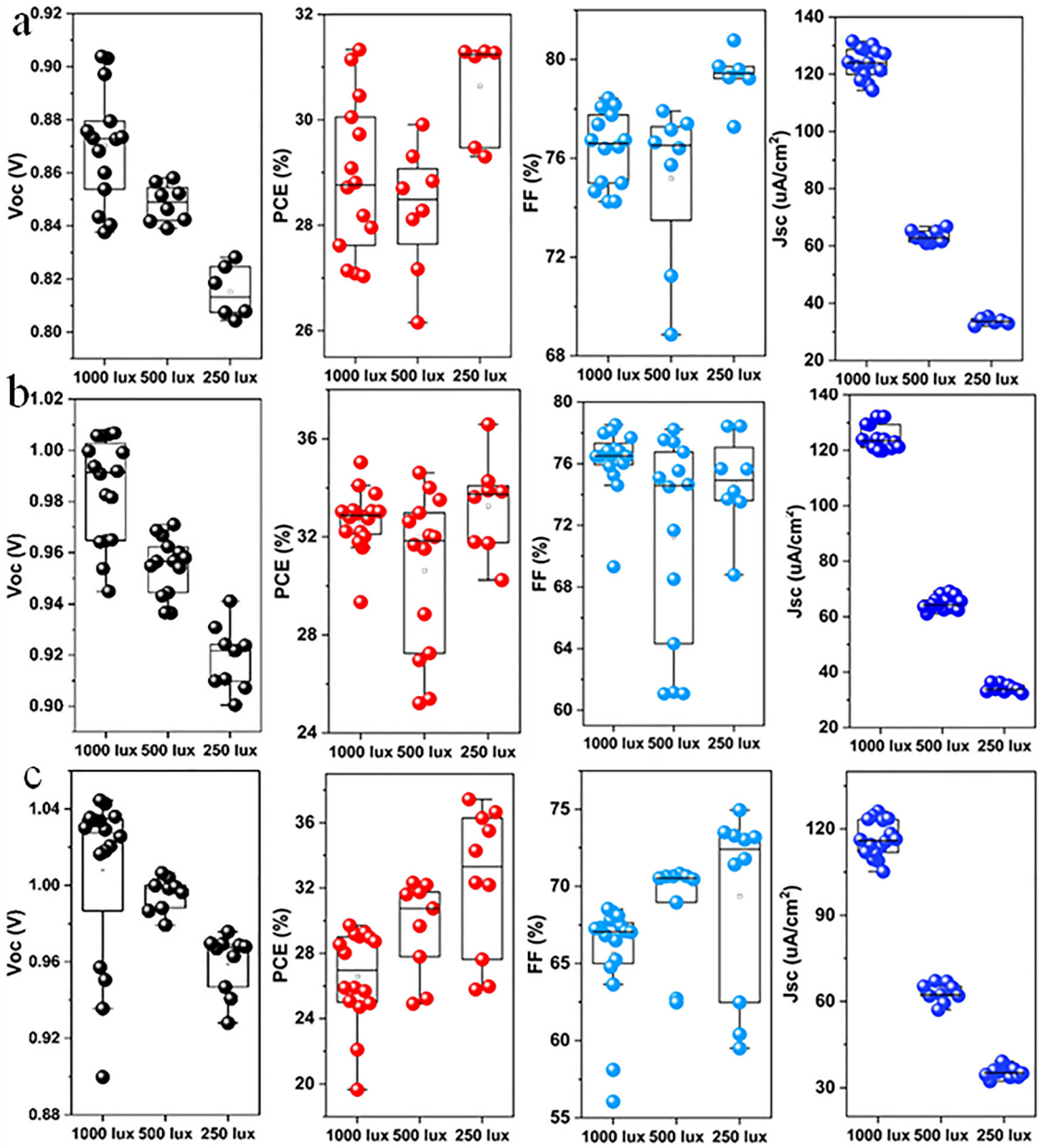

Fig. 3 Statistical analysis of the device's performance with (a) 1.55, (b) 1.72, and (c) 1.88 eV.

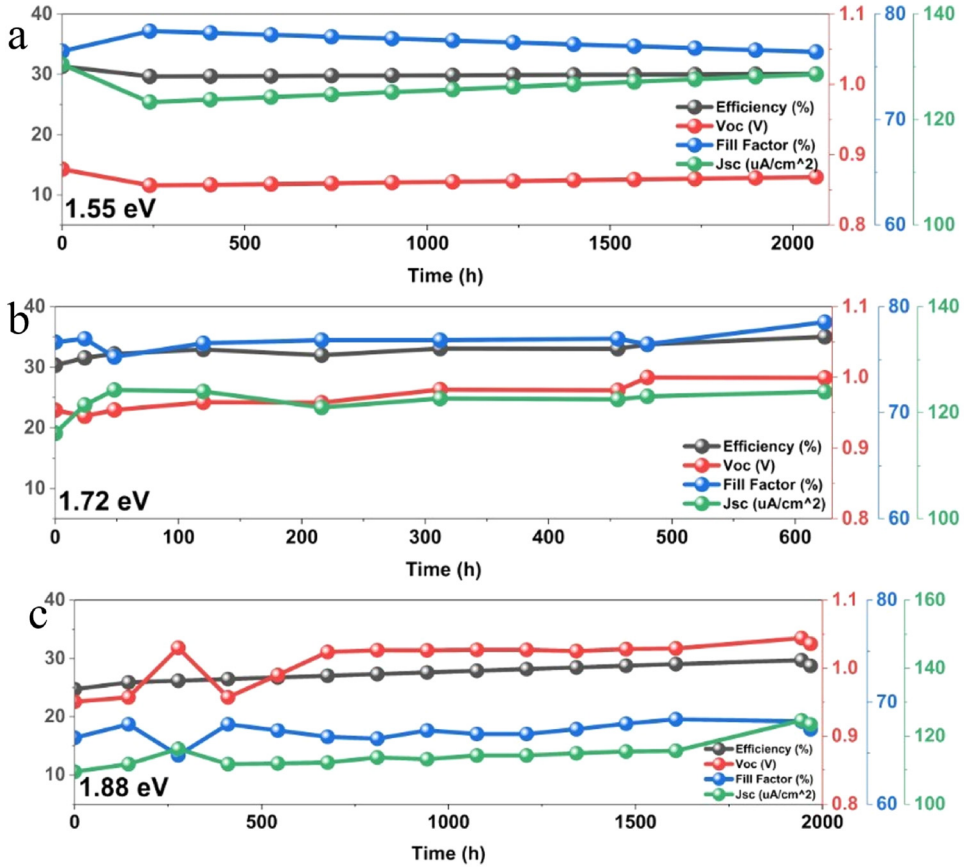

Fig. 4 The stability of the devices with (a) 1.55, (b) 1.72, and (c) 1.88 eV.

Conversely, the 1.88 eV absorber attained the highest V_{oc}, with efficiencies recorded at 27 ± 2.9% (1000 lux), 30.8 ± 2.9% (500 lux), and peaking at 33.3 ± 4.5% (250 lux). Overall, the findings substantiate the conclusion that the 1.72 eV composition provides a more reproducible performance across varying light conditions, while the 1.88 eV band gap variant provided the highest indoor efficiency of ~37% at low light intensity conditions.

Finally, stability assessments were conducted at an ambient temperature of 25 ± 5 °C, under relative humidity conditions of 30 ± 5%, and with illumination at 1000 lux, as depicted in Fig. 4a. The performance of the $FA_{0.85}Cs_{0.15}Pb(I_{0.55}Br_{0.45})_3$ (1.72 eV) device demonstrated notable improvements over a period exceeding 600 hours. Specifically, the PCE increased from 30.31% to 35.04%, accompanied by an enhancement in V_{oc} from 0.954 V to 0.999 V. The FF remained stable within the range of 77% to 78.5%, while the J_{sc} stabilized at approximately 124 μA cm^{-2}. In parallel, the $FA_{0.85}Cs_{0.15}Pb(I_{0.45}Br_{0.55})_3$ (1.88 eV) composition, illustrated in Fig. 4c, exhibited a similar performance trajectory over 2000 hours, with its PCE increasing from 25% to 29%, V_{oc} rising from 0.94 V to 1.04 V, J_{sc} improving from 114 to 124 μA cm^{-2} and FF increasing from 58% to 68%. The improved stability of the 1.72 eV and 1.88 eV devices is believed to arise from photo-induced defect passivation and halide redistribution under illumination, which reduced nonradiative recombination.[87] In the case of the 1.88 eV device, further enhancement is attributed to the gradual oxidation of Spiro-OMeTAD under illumination, which improves hole transport and fill factor.[44–46] Conversely, the $FA_{0.90}Cs_{0.10}Pb(I_{0.98}Br_{0.02})_3$ (1.55 eV) device, as shown in Fig. 4a, maintained stable performance throughout the 2000-hour duration, sustaining a PCE in the range of 29% to 30%. The observed stability of the 1.72 eV and 1.88 eV compositions presents an encouraging prospect for their application in indoor lighting.

Conclusion

This study investigated the compositional engineering of formamidinium-cesium-based perovskite $Cs_xFA_{x-1}Pb(I_{1-y}Br_y)_3$ for IPV applications. Through photoluminescence (PL) spectroscopy, three targeted bandgap energies of 1.55, 1.72, and 1.88 eV were successfully realized. Meanwhile, X-ray diffraction (XRD) revealed the effective incorporation of bromine into the crystal lattice, which surprisingly presented a suppressed δ-phase and PbI_2 impurities, which are reported systematically for indoor solar cell applications. Morphological analysis using scanning electron microscopy (SEM) and atomic force microscopy (AFM) revealed the formation of dense, pinhole-free films. However, a higher bromine content led to a reduced grain size and increased surface roughness due to rapid

crystallization. On one hand, this helped the devices to achieve high J_{sc}, but on the other hand it was identified (from simulations) as a limiting factor towards attaining the maximum possible indoor PCE. An optimal active layer thickness of 300–400 nm was established by using a precursor concentration of 1.3 M. Performance tests under different light intensities from white light-emitting diodes (WLEDs) revealed that among the wide band gap devices, the 1.72 eV bandgap composition had the highest J_{sc}, while the 1.88 eV band gap presented the highest V_{oc}. The device with a 1.88 eV bandgap achieved a notable indoor PCE of 37.4% at low light intensity (250 lux), surpassing the performance of other compositions. The 1.72 eV device, characterized by high values of J_{sc}, open circuit voltage (V_{oc}), and fill factor (FF), achieved PCEs of 36.6% under 250 lux and 35.04% under 1000 lux, establishing it as the optimal candidate for indoor energy harvesting applications over different indoor illumination conditions (intensity and color temperature).

Experimental and methods

Materials

All chemicals and materials used in this study were of analytical grade and used as received without further purification.

For the electron transport layer (ETL), titanium diisopropoxide bis(acetylacetonate) solution (75% in 2-propanol) and ethanol >99.8% were purchased from Sigma Aldrich and mesoporous TiO_2 paste (30NRD) from Greatcell Solar Materials Pty Ltd.

The perovskite layer material solvents are dimethylformamide >99.8% (DMF) and dimethyl sulfoxide >99.8% (DMSO) from Sigma Aldrich. Methylammonium chloride >99.99% (MACl) and formamidinium iodide >99.99% (FAI) were purchased from Greatcell Solar Materials Pty Ltd. Cesium iodide 99.999% (CsI) and lead iodide 99.999% (PbI_2), and lead bromide 99.999% ($PbBr_2$) were purchased from Alfa Acer.

Hole transport layer (HTL) SpiroOMe-TAD >99.8% was purchased from Xi'an Polymer Light Technology Corp. Acetonitrile and isopropanol and lithium bis(trifluoromethane) sulfonimide >99.9% were purchased from Sigma Aldrich.

Electrode material gold 99.999% (Au) was purchased from Plasmaterials, Inc.

Device fabrication

A TiO_2 compact solution was prepared with titanium diisopropoxide bis(acetylacetonate) solution (75% in 2-propanol) (600 μL and 400 μL acetylacetone) in 9000 μL ethanol and the mesoporous TiO_2 layer is diluted to a paste in ethanol (1 : 6 weight ratio) and spun at a rotation speed of 5000 rpm for 15 seconds, and subsequently sintered at 450 °C for 30 minutes in a dry atmosphere.

The perovskite layer was prepared with 1.3 M composition in 0.5 mL DMF : DMSO 4 : 1.

Three mixed-halide perovskite compositions were prepared with varying iodide–bromide ratios to study the effect of halide content on film quality and device performance. The compositions were $FA_{0.85}Cs_{0.15}Pb(I_{0.15}–Br_{0.85})_3$, $FA_{0.85}Cs_{0.15}Pb(I_{0.55}–Br_{0.45})_3$ and $FA_{0.90}Cs_{0.10}Pb(I_{0.98}–Br_{0.02})_3$.

For the $FA_{0.90}Cs_{0.10}Pb(I_{0.98}–Br_{0.02})_3$ composition, the precursor solution contained 14 mg of methylammonium chloride (MACl), 16.9 mg of cesium iodide (CsI), 4.8 mg of lead(II) bromide ($PbBr_2$), 96.9 mg of formamidinium iodide (FAI), and 299.3 mg of lead(II) iodide (PbI_2). For the $FA_{0.85}Cs_{0.15}Pb(I_{0.55}–Br_{0.45})_3$ composition, 14 mg of MACl, 25.3 mg of CsI, 107.2 mg of $PbBr_2$, 96.9 mg of FAI, and 168.1 mg of PbI_2 were used. Finally, for the $FA_{0.85}Cs_{0.15}Pb(I_{0.15}–Br_{0.85})_3$ composition, 14 mg of MACl, 25.3 mg of CsI, 202.8 mg of $PbBr_2$, 96.9 mg of FAI, and 45.8 mg of PbI_2 were used in 0.5 mL of solvent.

In all cases, the precursor solutions were stirred overnight to ensure complete dissolution and filtered with a 0.45 μm filter before film deposition at a speed of 5000 rpm for 40 seconds.

Passivation layer: 3 mg of *n*-octyl ammonium iodide (OAI) in 1 mL of isopropanol at a speed of 4000 rpm for 30 seconds.

The spiroOMe-TAD was doped with bis(trifluoromethylsulfonyl)imide lithium salt (24 μL of a solution of 520 mg of LiTFSI in 1 mL of acetonitrile) and 28.8 μL of 4-*tert*-butylpyridine in 1 mL of chlorobenzene and it was applied by spin-coating at 4000 rpm for 25 seconds.

Finally, an approximately 80–100 nm layer of gold (Au) was deposited by thermal evaporation, completing the device fabrication.

Scanning electron microscopy (SEM)

The morphological characteristics of the perovskite samples were investigated using a field-emission scanning electron microscope (JSM-6010PLUS/LV, JEOL Ltd) at an operating voltage of 10 keV.

Atomic force microscopy (AFM)

The surface morphology was studied using the Bruker dimension ICON AFM system.

X-ray diffraction (XRD)

The crystal structure was evaluated using X-ray diffraction with a Rigaku Mini Flex apparatus, with a scanning range set from 10° to 50°.

Steady-state photoluminescence (PL)

Spectra were acquired using a Horiba FL3C-222 system, with excitation at a wavelength of 450 nm.

The current–voltage (*J*–*V*) characteristics

J–*V* measurements of indoor PVK cells were recorded under indoor light using the ILS-30 standard spectrum simulator (Enlitech Technology). LEDs were stabilized for 30 min before recording the measurements. The devices were measured at 3000, 4000, and 5000 K under 1000 lux, 500 lux, and 250 lux. The aperture mask area was 1 cm^2.

Author contributions

E. A. A. conceived the idea of the work, designed and planned the experiments and supervised the work. M. S. A., F. I. A., T. F. A., and

A. S. A. fabricated and optimized the perovskite solar cell devices, did all the basic characterizations, analyzed the data and wrote the first draft with support from E. A. A., G. K., T. F. A. and N. R. A. E. A. A., G. K. and G. P. revised the first draft and contributed to the explanation of the results. G. P. performed the simulations and wrote the simulations part. H. A., A. H. S. and I. H. K. contributed to the results, discussion and work supervision. N. T., D. T., M. M. A. and A. A. were responsible for top-view SEM, cross-section AFM, PL measurement and analysis. All authors contributed towards the preparation of the manuscript and approved its submission.

Conflicts of interest

There are no conflicts to declare.

Data availability

The data supporting this article have been included as part of the supplementary information (SI). Supplementary information available. See DOI: https://doi.org/10.1039/d5ma01159k.

Acknowledgements

E. A. A. and M. S. A. gratefully acknowledge the support from King Abdulaziz City for Science and Technology (KACST), Saudi Arabia. A. H. S. and I. B. K. acknowledge the support from a research grant funded by the Research, Development, and Innovation Authority (RDIA) – Kingdom of Saudi Arabia – with grant number (12979-iau-2023-TAU-R-3-1-EI). G. K., N. T., K. P. and E. K. gratefully acknowledge the support from the action: ''Promotion of quality, innovation and extroversion in universities (ID 16289)'', ''SUB1.1 Clusters of Research Excellence – CREs'' and funded by the Special Account of the Ministry of Education, Religious Affairs and Sports within the framework of the National Recovery and Resilience Plan ''Greece 2.0'', with funding from the European Union – NextGenerationEU and co-financing from national resources (National Public Investments Program – VAT contribution). G. P. and M. K. gratefully acknowledge the Hellenic Foundation for Research and Innovation (HFRI) under ''Sub-action 2 for Funding Projects in Leading-Edge Sectors – RRFQ: Basic Research Financing (Horizontal support for all Sciences)'', MultiCool (15117). F. I. A. acknowledges the support from King Saud University, Saudi Arabia. A. H. acknowledges the ongoing Research funding program, (ORF-2026), King Saud University, Riyadh, Saudi Arabia.

References

1 Y. Galagan, Perovskite solar cells from lab to fab: the main challenges to access the market, *Oxford Open Mater. Sci.*, 2021, **1**(1), itaa007.
2 National Renewable Enery Laboratory. Best research-cell efficiency chart, 2025. https://www.nrel.gov/pv/cell-efficiency.html.
3 C. Teixeira, *et al.*, Fabrication of low-cost and flexible perovskite solar cells by slot-die coating for indoor applications, *Mater. Adv.*, 2023, **4**(17), 3863–3873.
4 A. A. Goje, *et al.*, Review of flexible perovskite solar cells for indoor and outdoor applications, *Mater. Renewable Sustainable Energy*, 2024, **13**(1), 155–179.
5 I. Mathews, *et al.*, Self-powered sensors enabled by wide-bandgap perovskite indoor photovoltaic cells, *Adv. Funct. Mater.*, 2019, **29**(42), 1904072.
6 H. Opoku, *et al.*, Perovskite photovoltaics for artificial light harvesting, *Chem. – Eur. J.*, 2022, **28**(30), e202200266.
7 A. Venkateswararao, *et al.*, Device characteristics and material developments of indoor photovoltaic devices, *Mater. Sci. Eng., R*, 2020, **139**, 100517.
8 N. K. Elangovan, *et al.*, Recent developments in perovskite materials, fabrication techniques, bandgap engineering, and the stability of perovskite solar cells, *Energy Rep.*, 2024, **11**, 1171–1190.
9 J. K. W. Ho, H. Yin and S. K. So, From 33% to 57%–an elevated potential of efficiency limit for indoor photovoltaics, *J. Mater. Chem. A*, 2020, **8**(4), 1717–1723.
10 M. E. E. Alahi, *et al.*, Integration of IoT-enabled technologies and artificial intelligence (AI) for smart city scenario: recent advancements and future trends, *Sensors*, 2023, **23**(11), 5206.
11 P. Taylor, *Internet of Things (IoT) Connected Devices Worldwide 2030*, Statista Inc., New York, 2023, https://shorturl.at/8qUWU.
12 J. Xu, *et al.*, Key parameters and thresholds values for obtaining high performance perovskite solar cells indoors from full Br compositional and bandgap engineering, *ACS Appl. Energy Mater.*, 2023, **6**(20), 10215–10224.
13 C. Zhang, *et al.*, Br vacancy defects healed perovskite indoor photovoltaic modules with certified power conversion efficiency exceeding 36%, *Adv. Sci.*, 2022, **9**(33), 2204138.
14 J. W. Lim, *et al.*, Unprecedentedly high indoor performance (efficiency > 34%) of perovskite photovoltaics with controlled bromine doping, *Nano Energy*, 2020, **75**, 104984.
15 W. Chen, K. T. Mularso, B. Jo and H. S. Jung, Indoor light energy harvesting perovskite solar cells: from device physics to AI-driven strategies, *Mater. Horiz.*, 2025, **12**(11), 3691–3711.
16 P. Gnanasekaran, *et al.*, Interfacial engineering using C-3 alkyl linker-based carbazole-derived SAM layers to achieve 41.77% indoor efficiency in wide-bandgap perovskite solar cells, *Small*, 2025, 2500983.
17 C. Dong, *et al.*, Lycopene-based bionic membrane for stable perovskite photovoltaics, *Adv. Funct. Mater.*, 2021, **31**(25), 2011242.
18 X. He, *et al.*, 40.1% record low-light solar-cell efficiency by holistic trap-passivation using micrometer-thick perovskite film, *Adv. Mater.*, 2021, **33**(27), 2100770.
19 Y. Li, *et al.*, *In situ* formation of 2D perovskite seeding for record-efficiency indoor perovskite photovoltaic devices, *Adv. Mater.*, 2024, **36**(1), 2306870.

20 Q. Ma, *et al.*, One-step dual-additive passivated wide-bandgap perovskites to realize 44.72%-efficient indoor photovoltaics, *Energy Environ. Sci.*, 2024, **17**(5), 1637–1644.
21 M.-J. Wu, *et al.*, Bandgap engineering enhances the performance of mixed-cation perovskite materials for indoor photovoltaic applications, *Adv. Energy Mater.*, 2019, **9**(37), 1901863.
22 A. Chakraborty, *et al.*, Photovoltaics for indoor energy harvesting, *Nano Energy*, 2024, 109932.
23 X.-X. Gao, *et al.*, Stable and high-efficiency methylammonium-free perovskite solar cells, *Adv. Mater.*, 2020, **32**(9), 1905502.
24 M. H. Miah, *et al.*, Band gap tuning of perovskite solar cells for enhancing the efficiency and stability: issues and prospects, *RSC Adv.*, 2024, **14**(23), 15876–15906.
25 K. T. Mularso, *et al.*, Recent strategies for high-performing indoor perovskite photovoltaics, *Nanomaterials*, 2023, **13**(2), 259.
26 L. Luo, *et al.*, Large-area perovskite solar cells with $Cs_xFA_{1-x}PbI_{3-y}Br_y$ thin films deposited by a vapor–solid reaction method, *J. Mater. Chem. A*, 2018, **6**(42), 21143–21148.
27 Z. Qiu, *et al.*, Recent advances in improving phase stability of perovskite solar cells, *Small Methods*, 2020, **4**(5), 1900877.
28 C. Polyzoidis, K. Rogdakis and E. Kymakis, Indoor perovskite photovoltaics for the internet of things—challenges and opportunities toward market uptake, *Adv. Energy Mater.*, 2021, **11**(38), 2101854.
29 K.-L. Wang, *et al.*, Perovskite indoor photovoltaics: opportunity and challenges, *Chem. Sci.*, 2021, **12**(36), 11936–11954.
30 L.-C. Chen, Z.-L. Tseng and J.-K. Huang, A study of inverted-type perovskite solar cells with various composition ratios of $(FAPbI_3)_{1-x}(MAPbBr_3)_x$, *Nanomaterials*, 2016, **6**(10), 183.
31 Z. Bi, *et al.*, High-performance large-area blade-coated perovskite solar cells with low ohmic loss for low lighting indoor applications, *Chem. Eng. J.*, 2022, **446**, 137164.
32 S. Huang, *et al.*, Enhancing indoor photovoltaic efficiency to 37.6% through triple passivation reassembly and n-type to p-type modulation in wide bandgap perovskites, *Adv. Funct. Mater.*, 2025, 2502152.
33 N. D. Pham, *et al.*, Enhanced Indoor Perovskite Solar Cell Performance via Additive Engineering, Australian PV Institute, *Proceedings of the Asia Pacific Solar Research Conference 2024*, Australian PV Institute, 2024.
34 D. P. Milyutin, *et al.*, Temperature–humidity wireless sensor powered by a wide-bandgap perovskite solar cell, *Appl. Phys. Lett.*, 2025, **127**(7), 073902.
35 R. Datt, *et al.*, Wide bandgap perovskite photovoltaic on rigid and flexible substrates for indoor light harvesting, *Appl. Phys. Lett.*, 2025, **127**(4), 043903.
36 V. R. Chappidi, R. K. Challa and S. S. K. Raavi, Optimized mixed halide triple cation perovskite based indoor photovoltaic device architecture with ultrahigh open circuit voltage and efficiency >42%, *Energy Technol.*, 2025, 2500067.
37 D. Li, *et al.*, Dual optimization via doping PCBM with diamine for efficient pure-iodide wide-bandgap perovskite solar cells, *Adv. Funct. Mater.*, 2025, e02847.
38 S. Shcherbachenko, *et al.*, High-bandgap perovskites for efficient indoor light harvesting, *Adv. Energy Sustainability Res.*, 2024, **5**(5), 2400032.
39 B. Orwat, *et al.*, Highly efficient indoor perovskite solar cells with 40% efficiency using perylene diimide-based zwitterionic cathode interlayers, *Small*, 2025, **21**(17), 2411623.
40 A. Sharma, A. A. Guaman and J. A. Röhr, On the role of color temperature and color rendering index of white-light LEDs on the theoretical efficiency limit of indoor photovoltaics, *arXiv*, 2025, preprint, arXiv:2506.20811, DOI: 10.48550/arXiv.2506.20811.
41 Y. Qi, *et al.*, Recent progress in indoor photovoltaics based on all-inorganic perovskites, *Appl. Phys. Lett.*, 2025, **127**(4), 040502.
42 J. E. Lee, *et al.*, Unraveling loss mechanisms arising from energy-level misalignment between metal halide perovskites and hole transport layers, *Adv. Funct. Mater.*, 2024, **34**(30), 2401052.
43 A. Sadhanala, *et al.*, Preparation of single-phase films of $CH_3NH_3Pb\ (I_{1-x}Br_x)_3$ with sharp optical band edges, *J. Phys. Chem. Lett.*, 2014, **5**(15), 2501–2505.
44 N. A. N. Ouedraogo, *et al.*, Oxidation of spiro-OMeTAD in high-efficiency perovskite solar cells, *ACS Appl. Mater. Interfaces*, 2022, **14**(30), 34303–34327.
45 S. Toikkonen, *et al.*, Is doping of spiro-OMeTAD a requirement for efficient and stable perovskite indoor photovoltaics?, *Adv. Devices Instrum.*, 2024, **5**, 0048.
46 L. Nakka, A. G. Aberle and F. Lin, Effects of overnight oxidation on perovskite solar cells with Co(III) TFSI co-doped spiro-OMeTAD, *Energies*, 2022, **16**(1), 354.
47 G. Perrakis, *et al.*, Solar photons beyond the band gap wavelengths: their effect on solution-processed solar cells, *Mater. Horiz.*, 2025, **12**, 2922–2934.
48 B. T. Muhammad, *et al.*, Halide perovskite-based indoor photovoltaics: recent development and challenges, *Mater. Today Energy*, 2022, **23**, 100907.
49 P. Kumari, S. Prasanthkumar and L. Giribabu, Recent progress on perovskite based indoor photovoltaics: challenges and commercialization, *Sol. Energy*, 2024, **284**, 113049.
50 P. Chenna, *et al.*, Perovskite white light emitting diodes: a review, *Mater. Today Electron.*, 2023, **5**, 100057.
51 P. Kumari, S. Prasanthkumar and L. Giribabu, Recent progress on perovskite based indoor photovoltaics: challenges and commercialization, *Sol. Energy*, 2024, **284**, 113049.
52 E. A. Alharbi, *et al.*, Cooperative passivation of perovskite solar cells by alkyldimethylammonium halide amphiphiles, *Joule*, 2023, **7**(1), 183–200.
53 K. A. Bush, *et al.*, Compositional engineering for efficient wide band gap perovskites with improved stability to photoinduced phase segregation, *ACS Energy Lett.*, 2018, **3**(2), 428–435.
54 W. Rehman, *et al.*, Photovoltaic mixed-cation lead mixed-halide perovskites: links between crystallinity, photostability and electronic properties, *Energy Environ. Sci.*, 2017, **10**(1), 361–369.

55 A. S. Alharbi, *et al.*, Stable perovskite solar cells with exfoliated graphite as an ion diffusion-blocking layer, *J. Mater. Chem. A*, 2024, **12**(45), 31301–31311.
56 M. Ahmad, *et al.*, Investigating the sequential deposition route for mixed cation mixed halide wide bandgap perovskite absorber layer, *Energies*, 2021, **14**(24), 8401.
57 B.-wook Park, *et al.*, Understanding how excess lead iodide precursor improves halide perovskite solar cell performance, *Nat. Commun.*, 2018, **9**(1), 3301.
58 L. Gil-Escrig, *et al.*, Efficient wide-bandgap mixed-cation and mixed-halide perovskite solar cells by vacuum deposition, *ACS Energy Lett.*, 2021, **6**(2), 827–836.
59 S. Svanström, *et al.*, Effect of halide ratio and Cs^+ addition on the photochemical stability of lead halide perovskites, *J. Mater. Chem. A*, 2018, **6**(44), 22134–22144.
60 J. Hidalgo, *et al.*, Br-induced suppression of low-temperature phase transitions in mixed-cation mixed-halide perovskites, *Chem. Mater.*, 2024, **36**(20), 10167–10175.
61 L. Srathongsian, *et al.*, Cs and Br tuning to achieve ultralow-hysteresis and high-performance indoor triple cation perovskite solar cell with low-cost carbon-based electrode, *iScience*, 2024, **27**(4), 109306.
62 Q. Jiang, *et al.*, Compositional texture engineering for highly stable wide-bandgap perovskite solar cells, *Science*, 2022, **378**(6626), 1295–1300.
63 U. D. Menda, *et al.*, High-performance wide bandgap perovskite solar cells fabricated in ambient high-humidity conditions, *Mater. Adv.*, 2021, **2**(19), 6344–6355.
64 S. A. Kulkarni, *et al.*, Bandgap tuning of lead halide perovskites using a sequential deposition process, *J. Mater. Chem. A*, 2014, **2**(24), 9221–9225.
65 S. Du, *et al.*, Impact of precursor concentration on perovskite crystallization for efficient wide-bandgap solar cells, *Materials*, 2022, **15**(9), 3185.
66 T.-B. Song, *et al.*, Perovskite solar cells: film formation and properties, *J. Mater. Chem. A*, 2015, **3**(17), 9032–9050.
67 Y. Li, R. Li and Q. Lin, Engineering the non-radiative recombination of mixed-halide perovskites with optimal bandgap for indoor photovoltaics, *Small*, 2022, **18**(26), 2202028.
68 T. Asada, *et al.*, Influence of the electron transport layer on the performance of perovskite solar cells under low illuminance conditions, *ACS Omega*, 2024, **9**(30), 32893–32900.
69 E. Q. Han, *et al.*, High-performance indoor perovskite solar cells by self-suppression of intrinsic defects via a facile solvent-engineering strategy, *Small*, 2024, **20**(4), 2305192.
70 M. Minbashi, *et al.*, Efficiency enhancement of CZTSSe solar cells via screening the absorber layer by examining of different possible defects, *Sci. Rep.*, 2020, **10**(1), 21813.
71 L. A. A. Pettersson, L. S. Roman and O. Inganäs, Modeling photocurrent action spectra of photovoltaic devices based on organic thin films, *J. Appl. Phys.*, 1999, **86**(1), 487–496.
72 J. J. Khanam and Y. F. Simon, Modeling of high-efficiency multi-junction polymer and hybrid solar cells to absorb infrared light, *Polymers*, 2019, **11**(2), 383.
73 C. K. Borah, *et al.*, Investigating the influence of ambient light spectrum on the thickness and band gap of halide-perovskite for indoor photovoltaic application, *Sol. Energy*, 2023, **265**, 112114.
74 P. F. Ndione, Z. Li and K. Zhu, Effects of alloying on the optical properties of organic–inorganic lead halide perovskite thin films, *J. Mater. Chem. C*, 2016, **4**(33), 7775–7782.
75 X. Wang, *et al.*, Highly efficient perovskite/organic tandem solar cells enabled by mixed-cation surface modulation, *Adv. Mater.*, 2023, **35**(49), 2305946.
76 T. Maksudov, *et al.*, 23.6% Efficient perovskite-organic tandem photovoltaics enabled by recombination layer engineering, *Mater. Sci. Eng., R*, 2024, **159**, 100802.
77 Z. Yang, *et al.*, Device physics of back-contact perovskite solar cells, *Energy Environ. Sci.*, 2020, **13**(6), 1753–1765.
78 M. Minbashi and E. Yazdani, Comprehensive study of anomalous hysteresis behavior in perovskite-based solar cells, *Sci. Rep.*, 2022, **12**(1), 14916.
79 D. Mora-Herrera, J. A. Polito-Lucas and M. Pal, Insights from theoretical modeling of cesium-formamidinium-based mixed-halide perovskite solar cells for outdoor and indoor applications, *ACS Omega*, 2024, **9**(46), 46157–46175.
80 T. I. Alanazi, *et al.*, Investigation of HTL-free perovskite solar cell under LED illumination: interplay between energy bandgap and absorber optimization, *Phys. Scr.*, 2024, **99**(5), 055542.
81 S. Manjhi, *et al.*, Unveiling the potential of $Cs_3Sb_2Cl_xI_{9-x}$-based solar cells for efficient indoor light harvesting: numerical simulation, *Adv. Theory Simul.*, 2024, **7**(9), 2400128.
82 R. K. Sharma, R. Keshri and S. Yadav, Computational modeling of $Cs_3Sb_2I_9$-based novel architecture under WLED illumination for indoor photovoltaic applications, *Opt. Quantum Electron.*, 2024, **56**(11), 1815.
83 D. P. Panda, *et al.*, DMSO-free tin halide perovskites for indoor photovoltaics, *ACS Energy Lett.*, 2025, **10**, 3789–3798.
84 M. van Eerden, *et al.*, Optical analysis of planar multicrystalline perovskite solar cells, *Adv. Opt. Mater.*, 2017, **5**(18), 1700151.
85 C. Chen, *et al.*, Achieving a high open-circuit voltage in inverted wide-bandgap perovskite solar cells with a graded perovskite homojunction, *Nano Energy*, 2019, **61**, 141–147.
86 R. Wang, *et al.*, Efficient wide-bandgap perovskite photovoltaics with homogeneous halogen-phase distribution, *Nat. Commun.*, 2024, **15**(1), 8899.
87 M. Jošt, Ž. Ajdič and M. Topič, Performance of triple-cation perovskite solar cells under different indoor operating conditions, *ACS Appl. Mater. Interfaces*, 2024, **16**(45), 62195–62202.